Global maps of aerosol single scattering albedo using combined CERES-MODIS retrieval

Archana Devi[1], Sreedharan K Satheesh[1,2,3]

[1] Centre for Atmospheric and Oceanic Sciences, Indian Institute of Science, Bengaluru, India
[2] Divecha Centre for Climate Change, Indian Institute of Science, Bengaluru, India
[3] DST Centre of Excellence in Climate Change, Indian Institute of Science, Bengaluru, India

Correspondence to: Archana Devi (archana.shiva13@gmail.com)

Abstract. Single Scattering Albedo (SSA) is a leading contributor to the uncertainty in aerosol radiative impact assessments. Therefore accurate information on aerosol absorption is required on a global scale. In this study, we have applied a multi-satellite algorithm to retrieve SSA (550 nm) using the concept of 'critical optical depth.' Global maps of SSA were generated following this approach using spatially and temporally collocated data from Clouds and the Earth's Radiant Energy System (CERES) and Moderate Resolution Imaging Spectroradiometer (MODIS) sensors on board Terra and Aqua satellites. Limited comparisons against airborne observations over India and surrounding oceans were generally in agreement within ±0.03. Global mean SSA estimated over land and ocean is 0.93 and 0.97, respectively. Seasonal and spatial distribution of SSA over various regions are also presented. The global maps of SSA, thus derived with improved accuracy, provide important input to climate models for assessing the climatic impact of aerosols on regional and global scales.

1 Introduction

Atmospheric aerosols play a significant role in the Earth's radiation budget (IPCC, 2013). The climatic impact of aerosols depends on their absorption and scattering properties, quantified by Single Scattering Albedo (SSA). Even a slight reduction in SSA can change the aerosol radiative forcing from cooling to warming, depending on the underlying surface albedo (Kaufman et al., 2001; Chand et al., 2009). However, the lack of an accurate global aerosol absorption database has led to SSA being the largest contributor to the total uncertainty in aerosol radiative impact assessment (IPCC, 2013).

The high spatio-temporal variability in aerosol properties entails the need for observations on a global scale (Dubovik et al., 2002; Levy et al., 2007; Remer et al., 2008; Hammer et al., 2018). Satellite data, despite its inherent limitation associated with an inverse problem, can provide the global perspective required in analysing

spatio-temporal aerosol characteristics (Torres et al., 2002; Lenoble et al., 2013). However, it is difficult to quantify the absorption over bright surfaces (Kaufman and Joseph, 1982; Ahn et al., 2014; Jethva et al., 2018). Hence, quantifying the aerosol absorption over land regions using satellite-based remote sensing remains a challenge even now (Torres et al., 2013; Jethva and Torres, 2019).

5   Fraser and Kaufman., 1985 developed a critical surface reflectance method to retrieve SSA using satellite data. Their method is based on radiative transfer simulations, which showed a particular surface reflectance for which the top of atmosphere albedo is independent of AOD. Upward radiances between a clear and a hazy day over a varying surface reflectance region are used, along with radiative transfer simulations, to derive SSA. This method has been widely applied to data from various satellites to derive SSA over particular regions (Kaufman, 1987; 10   Kaufman et al., 1990, 2001; Zhu et al., 2011; Wells et al., 2012). Seidel and Popp., 2012 have done extensive studies on the method's sensitivity to various parameters.

Various studies have ascertained the inadequacy of single-sensor data in the accurate retrieval of aerosol absorption (Kaufman et al., 2001; Zhu et al., 2011). Dawn of the A-Train satellite constellation (Anderson et al., 2005) with spatially and temporally near-collocated observations facilitates multi-satellite retrieval of aerosol 15   absorption (Eswaran et al., 2019; Hsu et al., 2000; Hu et al., 2007, 2009; Jeong and Hsu, 2008; Narasimhan and Satheesh, 2013; Satheesh et al., 2009) However, all these multi-sensor retrievals are in the Ultra Violet (UV) wavelengths, and SSA is extrapolated to visible wavelengths using spectral dependence of assumed particle size distribution. Satheesh and Srinivasan (2005) defined the concept of "critical optical depth" (τ_c) and introduced a method to retrieve SSA in the visible region by combining ground-based and satellite measurements. The method 20   was validated/demonstrated over many locations, including the desert location of Solar Village in Saudi Arabia, using Aerosol Robotic Network (AERONET) data.

In this paper, we have utilized the concept of τ_c and further extended the methodology to develop the combined CERES-MODIS retrieval algorithm to derive regional and global maps of aerosol absorption (550 nm) using multi-satellite data. The "critical optical depth" method developed in this research paper shares a similar concept 25   to the critical surface reflectance method (Fraser and Kaufman., 1985). For a particular parameter (such as surface reflectance or optical depth), there exists a critical value at which the top of atmosphere albedo can be considered independent of variations in that parameter. Both the methods retrieve SSA by parameterizing the critical value as a function of SSA using radiative transfer simulations. The critical reflectance method requires two-days data and large variations in surface reflectance over the region. It's suitable for retrieving daily SSA for a particular

region. Whereas the critical optical method developed in this paper is suitable for retrieving monthly or seasonal global maps of SSA.

The concept of τ_c, which forms the scientific basis for the development of this retrieval algorithm is illustrated in Section 2. The various steps involved in the retrieval algorithm are detailed in the Section 3, data and methodology. Section 4 presents the results and comparison with other satellite datasets. Uncertainity analysis is studied in Section 5. Comparison with aircraft measurements from various field campaigns are shown in Section 6. Comparison with AERONET data from 15 sites are shown in section 7. Summary and conclusions are provided in Section 8.

2 Critical optical depth

Let $\Delta\alpha$ be the difference between the top of the atmosphere (TOA) albedo and surface albedo. Then, for a particular location, with a given surface albedo, $\Delta\alpha$ variations are only due to changes in TOA albedo. The presence of absorbing aerosols over a bright surface decreases the TOA albedo. In contrast, scattering aerosols over a dark surface increase the TOA albedo. Thus, the increase (decrease) in aerosol loading due to scattering (absorbing) type of aerosols leads to an increase (decrease) in $\Delta\alpha$. The rate of change in $\Delta\alpha$ with aerosol loading is dependent on SSA.

Satheesh and Srinivasan (2005) utilized this concept to retrieve SSA in the case of absorbing aerosols over a bright surface. In a pristine atmosphere (Aerosol Optical Depth = 0) over a bright surface, the $\Delta\alpha$ is positive for solar zenith angle (SZA) = 0. Here, when absorbing aerosols become dominant, $\Delta\alpha$ decreases with an increase in aerosol optical depth (AOD) and eventually turns negative. The AOD at which $\Delta\alpha$ equals zero is defined as τ_c. For a given surface albedo, τ_c is the AOD at which the scattering and absorbing effects of the aerosol cancel each other. The rate of decrease in $\Delta\alpha$ with the increase in AOD is higher when SSA is high and consequently lowers the resulting values of τ_c. A radiative transfer (RT) model was then used to calculate the SSA that reproduces the same τ_c, given atmospheric conditions.

Figure 1. RT simulations (black dots) shows deriving τ_c (red dot) for different cases of aerosols and surfaces. For pristine conditions (AOD = 0), diurnally-averaged $\Delta\alpha$ is negative for bright surfaces and positive for dark surfaces. An increase in aerosol loading by absorbing (scattering) type of aerosol leads to decrease (increase) in TOA albedo. **(a)** Absorbing aerosols above a dark surface; **(b)** Absorbing aerosols above a bright surface; **(c)** Scattering aerosols above a dark surface; **(d)** Scattering aerosols above a bright surface.

In this paper, the concept of τ_c is extended to retrieve SSA for all scenarios of surfaces (dark and bright) and aerosols (absorbing and scattering). For AOD less than 1, $\Delta\alpha$ is almost linearly dependent on AOD. Then τ_c is mathematically the x-intercept when parameterizing the linear relationship.

5   Figure 1 shows the estimation of τ_c for four different scenarios. Details of these RT simulations are given in Section 3.2. Unlike Satheesh and Srinivasan (2005), where simulations were carried out for SZA = 0, here the $\Delta\alpha$ is diurnally averaged. Therefore, it is possible to have negative $\Delta\alpha$ for AOD = 0 over relatively bright surfaces. It is difficult to retrieve SSA where the slope of regression line is close to zero.

3 Data and methodology

The Combined CERES-MODIS retrieval algorithm consists mainly of two steps: (1) determining τ_c using MODIS and CERES data for a location, and (2) estimation of SSA that reproduces the same τ_c for the associated atmospheric conditions and surface albedo of that particular location. Figure 2 shows the flowchart illustrating the combined CERES-MODIS retrieval algorithm.

TOA and surface fluxes, used to determine $\Delta\alpha$, are obtained from CERES SYN1deg-day (Edition 4.1) (Wielicki et al., 1996; Rutan et al., 2015). To avoid angular dependence of fluxes, the diurnally averaged flux data product from CERES is used, which is available only at 1° resolution. Hence, other satellite data sets in this study are also used at the same spatial resolution. AOD and total columnar water vapor are obtained from the MODIS Daily Global Product (MxD08_D3 version 6.1). MODIS retrieves columnar AOD at 550 nm using two different types of algorithms – "Dark Target" (Levy et al., 2007, 2013) and "Deep Blue" (Hsu et al., 2004, 2006; Sayer et al., 2013). Dark target retrieves AOD over both land and ocean, whereas deep blue retrieves only over land. In this study, we have used a combined dark target and deep blue product.
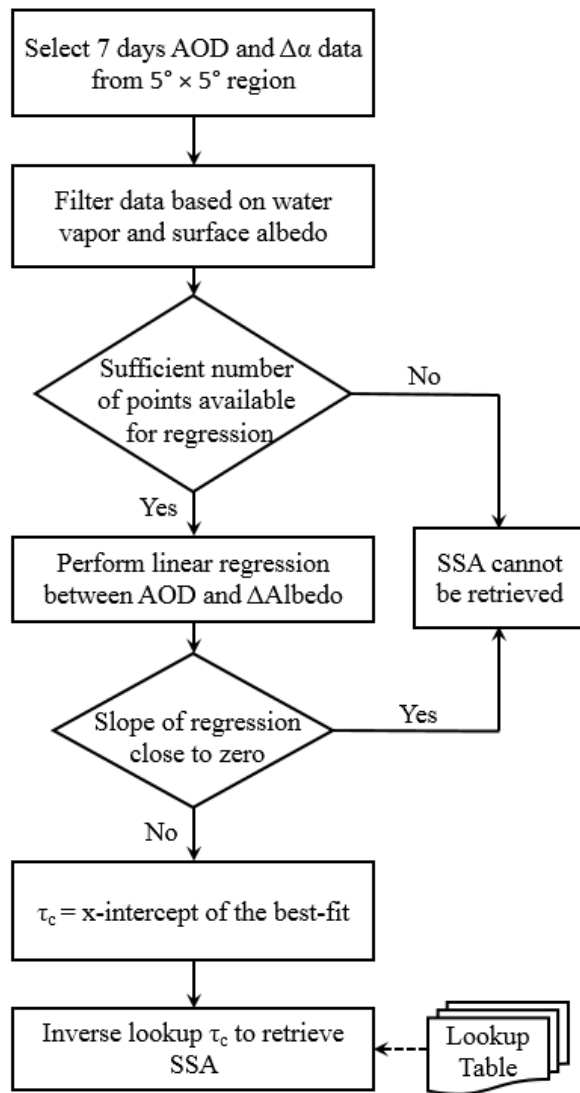
Figure 2. Flowchart depicting the steps involved in combined CERES-MODIS retrieval of SSA for a particular location.

3.1 Determining the critical optical depth

The first step for retrieval is to determine τ_c by linear regression analysis between $\Delta\alpha$ vs. AOD as shown in Fig. 3. The x-intercept of the resultant line of best fit (i.e., the AOD at which $\Delta\alpha = 0$) provides the value of τ_c. CERES

and MODIS daily data are at 1° resolution, and SSA is retrieved for each 1° × 1° grid. In order to have adequate number of points for a meaningful regression analysis, it was required to use data over a larger interval (temporal and spatial) - whose extent is large enough to get a statistically significant fit but small enough to ensure insignificant variations in SSA. Thus, to determine τ_c for a given pixel, seven days of data from its surrounding

5   5° × 5° region has been considered. This data is further constrained based on surface albedo and water vapor. Only those pixels in this region having surface albedo within $\pm$ 0.025 and water vapor within $\pm$ 0.25 cm of the given pixel are considered for regression analysis. These constraints ensure that the τ_c determined from the best fit is dependent only on SSA and not affected by changes in surface albedo and water vapour. Figure 3a shows an example of regression with a positive correlation coefficient over the Arabian Sea. This can happen over regions

10   of low surface albedo and the dominance of scattering aerosols. Figure 3b is an example of regression analysis with a negative correlation coefficient obtained over Sahara in the presence of dust aerosols.

The above procedure is repeated for all pixels, where data from the surrounding 5° × 5° region is used to determine τ_c for each pixel. For the regression analysis, points which are outside one standard deviation are considered as outliers. Line of best fits with a slope close to zero yields extreme τ_c values (very high positive/very low negative). In such cases, we did not attempt a retrieval. A significance test on the correlation coefficient between AOD and

15   ΔAlbedo is performed with a 0.05 significance level. Only those τ_c values obtained through regressions that are statistically significant at 95% confidence level are utilized further to retrieve SSA.
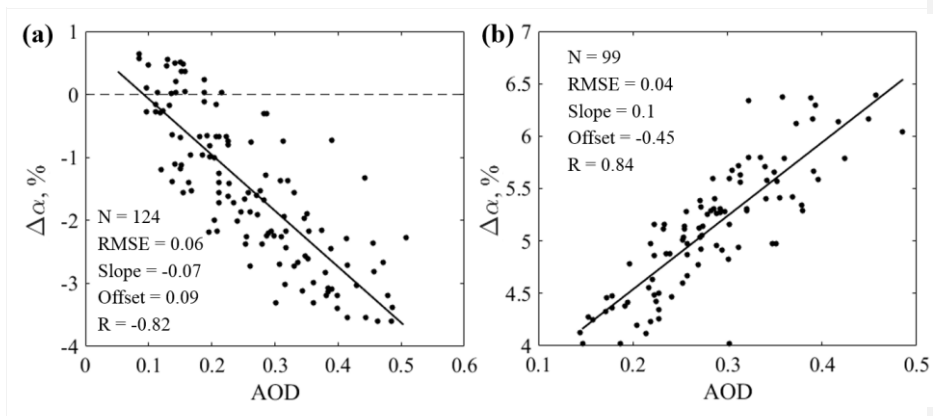
Figure 3. Sample scatterplots between MODIS AOD and CERES $\Delta\alpha$. The solid lines represent the best-fits for **(a)** absorbing aerosols above the Sahara and **(b)** scattering aerosols above the Arabian Sea. τ_c (AOD at which $\Delta\alpha$ is zero) is the x-intercept of the best-fit line.

The final product of this step is a 360×180 matrix that stores τ_c value corresponding to each 1° pixel. In these matrices, not all points would have a τ_c value owing to the insufficient number of points available for regression, either due to cloud-masking or large variations in surface albedo over the land. At least seven days of data is required to perform a statistically significant fit to compute τ_c and retrieve SSA The next step in the procedure is to estimate SSA from these τ_c values using an inverse lookup table (LUT) approach.

3.2 Retrieval of SSA

Since the objective of this study is to retrieve SSA globally, look-up-tables (LUTs) were developed to reduce the computation time and avoid repeated RT simulations. The aerosol models from OPAC (Optical Properties of Aerosols and Clouds), developed by Hess et al., (1998), are given as input to SBDART (Santa Barbara DISORT Atmospheric Radiative Transfer) model (Ricchiazzi et al., 1998) to simulate TOA fluxes. Specifications of the model used are shown in Table S5, S6 and S7.

The RT computations were carried out to obtain the diurnally averaged (SZA: 0° to 84°) TOA and surface fluxes using 16 radiation streams and spectrally integrated over the shortwave region (0.3 to 5 μm). For a particular case of surface albedo, water vapor, and SSA, AOD is varied from 0 to 1 in steps of 0.2 to generate its corresponding diurnally averaged $\Delta\alpha$. Then a linear fit is performed between AOD and simulated $\Delta\alpha$ to determine τ_c. A three-dimensional LUT that stores τ_c for different combinations of surface albedo, water vapor, and SSA have been developed. The LUT is indexed by 11 values of surface albedo (0 to 0.5, increments of 0.05), 17 values of water vapour (0 to 8 cm, increments of 0.5 cm) and 10 values of SSA (0.8, 0.83, 0.85, 0.87, 0.9, 0.92, 0.95, 0.97, 0.99, and 1). A total of 89760 RT simulations were performed in the present study.

The next step is to estimate SSA from τ_c using the LUT. For a given surface albedo and water vapor of that pixel, we find the SSA associated with its determined τ_c. An inverse lookup operation is performed on LUT by linear interpolation between the nearest two indices. SSA is estimated for each available τ_c values of a pixel and then averaged to compute the seasonal mean SSA.

4 Results and discussion

Fig. 4 shows the seasonal-mean global maps of SSA (550 nm) retrieved by the combined CERES-MODIS algorithm for the five years of 2014-2018. Data are averaged for different seasons: DJF (December-January-February), MAM (March-April-May), JJA (June-July-August), and SON (September-October-November).
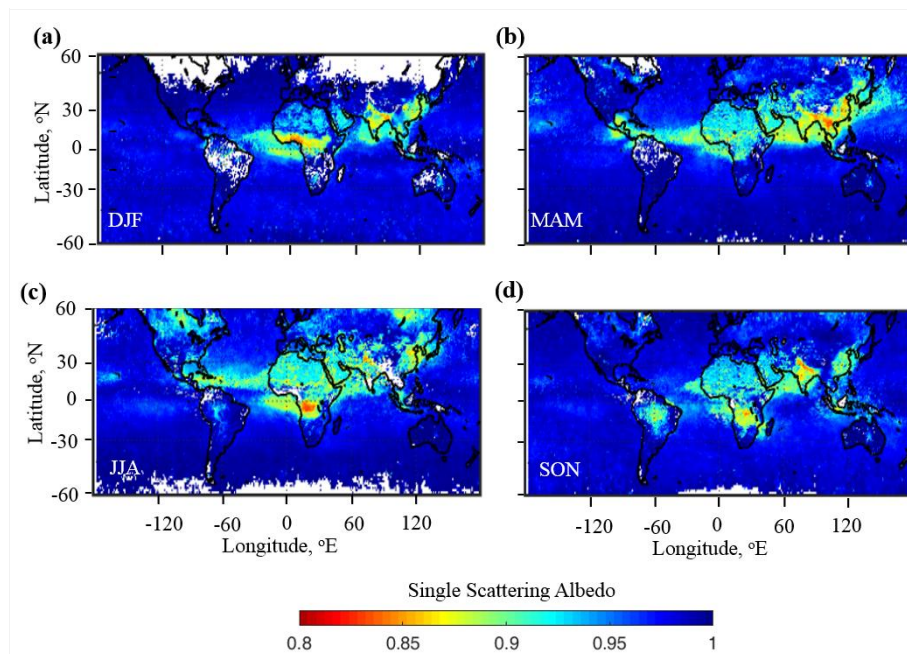
Figure 4. Seasonal mean SSA maps for the period of 2014-18 retrieved by the combined CERES-MODIS.

The retrieved SSA dataset (500 nm) was compared with other widely used global SSA datasets – OMI SSA (500 nm) and climatological POLDER SSA (565 nm). OMAERUVd V3 (Torres et al., 2007; Torres et al., 2013; Ahn et al., 2014) for the corresponding period are shown in panels a, c, e, and g in Fig 5. And POLDER 1-2 Level 3 climatological seasonal mean SSA maps are shown in panels b, d, f, and h in Fig 5. For a generalized qualitative comparison, we can assume that SSA does not vary much for the small 50 nm spectral difference between CERES-MODIS and OMI SSA. (Zhu et al., 2011; Jethva et al., 2014).
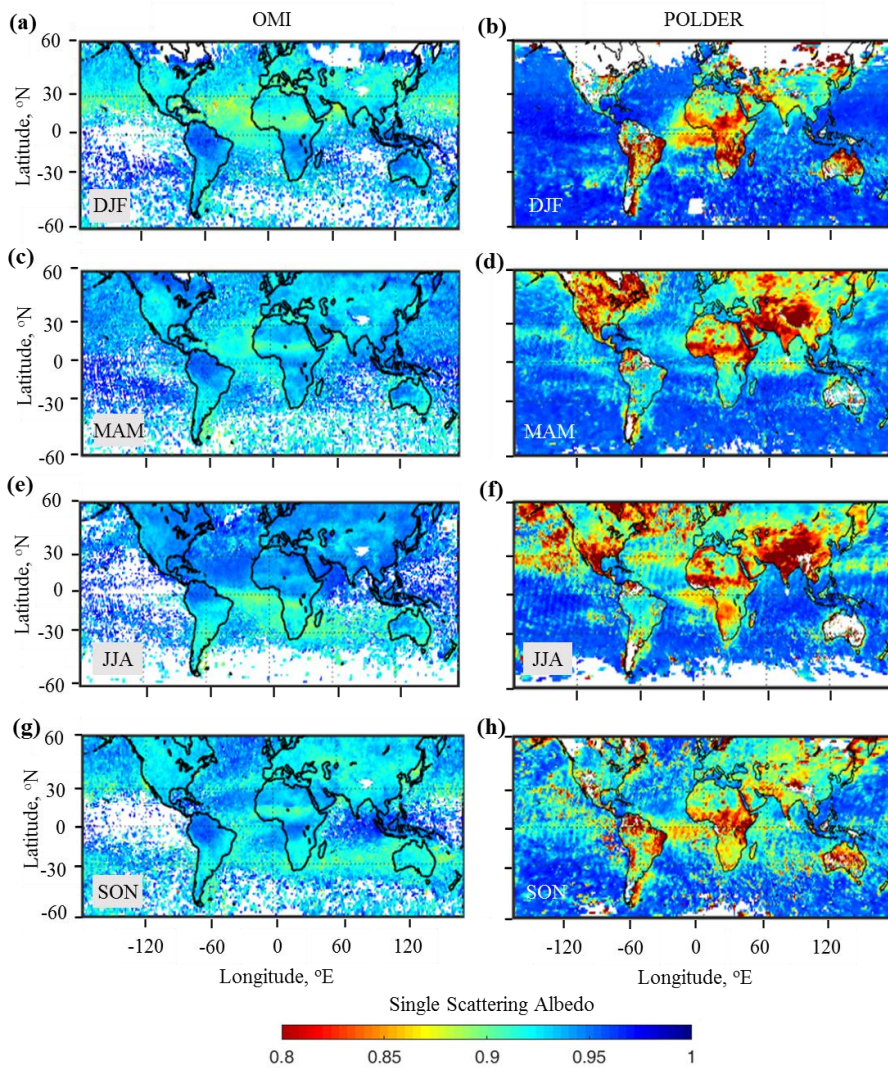
Figure 5. Seasonal mean SSA maps of OMI (500 nm) and POLDER (565 nm) in panels a,c,e,g and b,d,f,h respectively.

From a quick comparison between Fig 4 and Fig S2 SSA maps, the following points can be noted:

- Over the ocean, OMI retrieves SSA only for regions with high values of UVAI, leading to large data gaps. In comparison, we can notice that CERES-MODIS and POLDER have better data coverage on a global scale. In the CERES-MODIS maps, the absence of data is mostly due to the unavailability of MODIS AOD.

- The Global Ocean, a relatively dark surface covering more than 70% of the Earth's surface, plays a significant role in determining global aerosol radiative forcing effects. Therefore, the better data coverage over oceans by the CERES-MODIS and POLDER provides better input for radiative forcing calculations.

- CERES-MODIS maps capture a wider range of SSA values. Regions with very low SSA can easily be identified as the sources of absorbing aerosols. OMI SSA values are mostly above 0.9 and do not clearly capture the sources and transport of absorbing aerosols.

- Both POLDER and OMI SSA values are more accurate in the UV wavelengths since SSA is primarily retrieved in the UV regions and extrapolated to visible wavelengths using aerosol models. Whereas CERES-MODIS retrieves SSA directly at 550 nm, hence is more accurate for SSA values in the visible wavelengths.

- Over the land, POLDER shows very low SSA values (< 0.85), thus indicating the presence of highly absorbing aerosols even over less polluted regions. OMI values are around 0.9 over land and do not clearly identify the presence of absorbing aerosols. Whereas SSA values are within reasonable range over land as retrieved by the CERES-MODIS method – high SSA values over relatively pristine regions, lower SSA values over sources and transport of absorbing aerosols.

- Seasonal trends in forest fire can be noticed in POLDER maps and distinctly identifiable in CERES-MODIS SSA maps. Every year forest fires are common in specific seasons in Canadian and Russian Boreal forests (JJA), Amazon forest (SON) and South African forest (JJA and SON).

- The Indo-Gangetic plain (IGP) is a densely populated region spotted with several coal-based thermal power plants and seasonal stubble burning. Low SSA values are retrieved by both POLDER and CERES-MODIS over IGP. Whereas OMI shows values around 0.9 throughout the year. Similar pattern can be observed over Eastern China, one of the most highly polluted industrial region.

From the above points, we can draw conclusions about the advantages of each dataset. OMI, CERES, and MODIS instruments are still operational, whereas POLDER datasets are available only till 2013. OMI and POLDER SSA datasets are more suitable for UV wavelengths, whereas the CERES-MODIS SSA dataset provides more accurate SSA over visible wavelengths. OMI provides operational daily global SSA maps, whereas the CERES-MODIS algorithm is more suitable for obtaining monthly/seasonal global SSA maps. Over the ocean, the POLDER dataset has more coverage than OMI and identifies the transport of aerosols across the oceans. Hence, POLDER SSA and CERES-MODIS SSA can be used for studying SSA values over the ocean in the UV and visible wavelengths, respectively. Over the land, OMI retrieves high SSA values, whereas POLDER shows very low SSA values even over relatively pristine regions. Hence, the CERES-MODIS dataset retrieves reasonable SSA values over both polluted and less polluted regions for visible wavelengths.

Global mean SSA retrieved by combined CERES-MODIS over land and ocean is 0.93 and 0.97, respectively (OMI: 0.94 and 0.94). Accurate SSA estimations are also required over regions of interest such as deserts, oceans, biomass-burning forests, and highly polluted industrial areas. Hence, seasonal mean SSA values retrieved by the combined CERES-MODIS algorithm, OMI, and POLDER are reported, in table S2, for major regions of interest as shown in Fig S1 and Table S1.

5 Uncertainty Analysis

Table 1 identifies the major sources of error in the retrieval and summarizes their individual contribution. Uncertainty in the retrieved SSA was estimated by calculating retrieval sensitivities to perturbations in the possible error sources. The range of perturbation was based on published literature or reasonable assumptions for possible variations.

Table 1. Estimates of the uncertainty in retrieved SSA

Parameter	Input Uncertainty	Retrieval Uncertainty
Surface albedo	±0.01	±0.03
AOD	20% ±0.05 (land) 5% ±0.03 (ocean)	±0.02
Angstrom exponent	±0.4	±0.01
Refractive index	±0.01	±0.01
Aerosol height	±1 km	±0.01
Aerosol type	Smoke vs dust	±0.01
Residual of fit	±0.05	±0.02

Uncertainty in shortwave integrated surface albedo from CERES results in the maximum uncertainty in SSA of ±0.03. MODIS retrieved aerosol optical depth contains considerable uncertainties due to assumed aerosol models (Jeong et al., 2005). The MODIS aerosol optical depth uncertainty is 20% ±0.05 over land (Chu et al., 2002) and 5% ±0.03 over the ocean (Remer et al., 2002). The corresponding error in our retrieval is ±0.02. For a typical variation of angstrom exponent (±0.4) and refractive index (±0.01), the uncertainties vary depending on the surface albedo and are mostly around ±0.01.

Changes in aerosol height can vary the TOA radiances due to Rayleigh scattering interactions, which depend on pressure. Sensitivity to aerosol height was estimated by conducting a synthetic retrieval of SSA over a range of aerosol height values and perturbations from those heights. The average uncertainty observed for an aerosol height variation of ±1 km was ±0.01. Many methods have been developed for detecting aerosol type, especially smoke vs. dust, to improve the uncertainties of various AOD and SSA retrievals.

Uncertainties due to possible variations on scales of the regions used for linear fitting were estimated as residuals of the fit. The uncertainty on the linear intercept is spatially dependent and is mostly around ±0.02, with higher values for those combinations having a slope close to zero during the regression. For highly correlated cases (i.e., correlation coefficient | r | > 0.5), the probability of obtaining a slope close to zero is ~20% over the ocean and <5% over land. These cases are mostly formed over regions where AOD variations are less. Regions having large variations in AOD values have lower uncertainty due to residual fit.

Overall, the algorithm is most sensitive to variations in surface albedo, followed by higher sensitivity towards AOD values used in the linear fit. Seaonal mean maps of surface albedo are shown in Fig S3. The uncertainties are higher for scattering aerosols over bright surfaces and absorbing aerosols above dark surfaces. Sensitivity to water vapor is almost negligible, except in very few cases where the uncertainty is + 0.008. The CERES-MODIS algorithm is most effective over regions with large AOD variations and less surface albedo variations.

6 Comparison with airborne observations

For the comparison of columnar SSA values thus retrieved, we have used aircraft-based measurements of SSA from three campaigns: South West Asian Aerosol Monsoon Interactions (SWAAMI), Regional Aerosol Warming Experiment (RAWEX), and SWAAMI-RAWEX, to obtain column-integrated SSA. Available data points over India and adjoining oceanic regions (Arabian Sea and Bay of Bengal) from these field campaigns were compared with the retrieved SSA.

Deleted: 4

Deleted: Validation

Babu et al. (2016), as part of RAWEX (Moorthy et al., 2016), derived SSA at 520 nm from aircraft measurements of scattering and absorption coefficients over the Indo-Gangetic Plain (IGP) and Central India during winter 2012 and spring/pre-monsoon 2013. Various measurements of aerosol properties were carried out in an instrumented Beechcraft B200 aircraft of the National Remote Sensing Centre, India. Manoj et al. (2019) estimated vertical profiles of SSA during the SWAAMI campaign conducted during monsoon (June - July) 2016 over IGP, Arabian Sea, and Bay of Bengal. Aerosol scattering coefficients were measured aboard the Facility for Airborne Atmospheric Measurements (FAAM) BAe-146 aircraft. Vaishya et al. (2018) estimated vertical profiles of SSA (520 nm) using an instrumented aircraft, Beechcraft B200, during SWAAMI-RAWEX campaign (June 2016). Instrument design and calibration were based on Anderson et al., 1996 and its application for Indian field experiments was as described by Nair et al., 2009. Uncertainties in the scattering coefficient measurement by nephelometer are ~±10%, as reported by Anderson et al., 1996. As stated by Babu et al., 2016 uncertainties in the columnar SSA values estimated from RAWEX aircraft measurements depend mainly on instrumental uncertainties, sampling errors, and large spatial averaging.

Retrieved SSA, for the same period as the campaign, over a 2°×2° region around the campaign location was utilized for comparison. Figure 4 shows the comparison of collocated aircraft measurements and CERES-MODIS retrieved SSA. The ideal 1:1 case (solid line), the absolute difference of 0.03 (dotted lines), and regression coefficients are also provided.
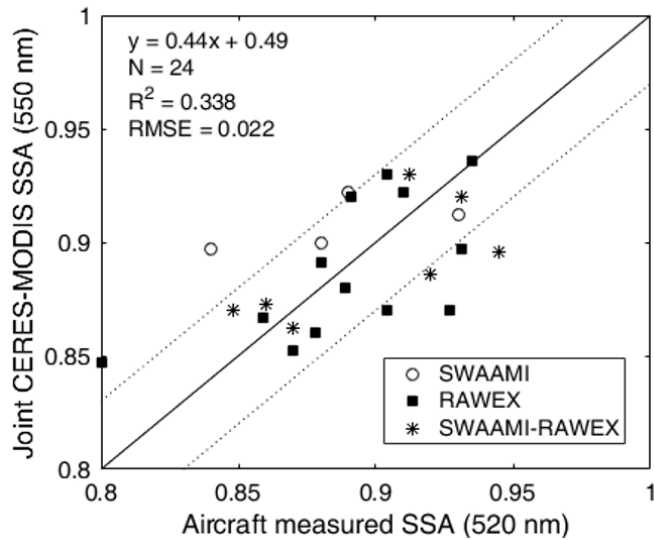
Figure 6. Comparison of combined CERES-MODIS SSA with aircraft measurements during SWAAMI, RAWEX, and SWAAMI-RAWEX campaigns. The solid line shows the ideal 1:1 case and dotted lines represent the absolute difference of 0.03.

Most of the points were within the absolute difference of 0.03. However, there are few exceptions. SSA values over the Bay of Bengal during SWAAMI campaign were reported as 0.84 ± 0.07 during June-July by Manoj et al. (2019), whereas CERES-MODIS retrieves a higher SSA of ~0.89 for the same time period. This large variation

5   could be due to frequent cloud cover during the monsoon season, leading to fewer SSA points retrieved over the ocean and land. SSA estimated over Nagpur in Central India during RAWEX is ~0.8, while CERES-MODIS retrieves ~0.85. This inconsistency is due to the large surface albedo variations (standard deviation >0.05) over Central India, which leads to fewer points available for retrieval. Except for few such cases, most of the other points lie within an absolute difference of 0.03.

10   For comparison purposes, many previous studies have used ground-level SSA data from AERONET obtained through inversion methods (Zhu et al., 2011; Jethva et al., 2014). Even in this study, only very few points were available for comparsion due to the limited number of direct measurements of columnar SSA. Despite this limitation, this comparison exercise provided confidence to generate global maps of SSA following this method.

7 Comparison with AERONET data

The Aerosol Robotic Network is a ground-based worldwide federated network of Cimel Sun photometers that measure extinction AOD from direct Sun measurements (Holben et al., 1998). The spectral diffuse sky radiations measured at different angles are inverted in conjunction with direct Sun measurements to derive the spectral SSA (440, 675, 870, and 1020 nm) and size distribution (Dubovik and King., 2000). The estimated uncertainty in retrieved SSA is largely attributed to the uncertainties in instrument calibration and is within 0.03 for AOD (440 nm) larger than 0.4. (Dubovik et al., 2000,2002).

AERONET version 3, level 2.0 monthly average values from selected sites were compared with corresponding CERES-MODIS SSA data. Sites were chosen to represent various types of aerosols following that of Giles et al., 2012. The location of the sites is shown in Fig S2 and Table S3. Scatter plots of comparison of AERONET SSA (440 nm) and CERES-MODIS SSA (550 nm) are shown in Fig 7.

Most AERONET SSA values are above 0.85, even in case of biomass burning aerosols. For dust type of aerosols (sites: Capo_Verde, Dakar and Banizoumbaou), as shown in Fig 7a, AERONET and CERES-MODIS have better agreement. Whereas, in case of mixed type of aerosol (sites: SEDE_BOKER, Kanpur, Xiang He and Illorin), most of the CERES-MODIS values are below 0.85, indicating highly absorbing type of aerosols (Fig 7b). For urban (sites: GSFC, Mexico_city, Shirahama, Ispra and Moldova) and biomass (sites: Alta_Floresta, Lake_Argyle and Mongu) only very few data were available during the study period of 2014-18 as shown in Fig 7 panels c and d. Data points combined from all the sites are plotted together in Fig 7e showing a RMSE of 0.037. The large difference between SSA wavelengths of AERONET (440 nm) and CERES-MODIS (550 nm) could contribute to the variations observed between these two datasets. Overall, the resulting comparisons are agreeable within the uncertainties of both AERONET and CERES-MODIS datasets.
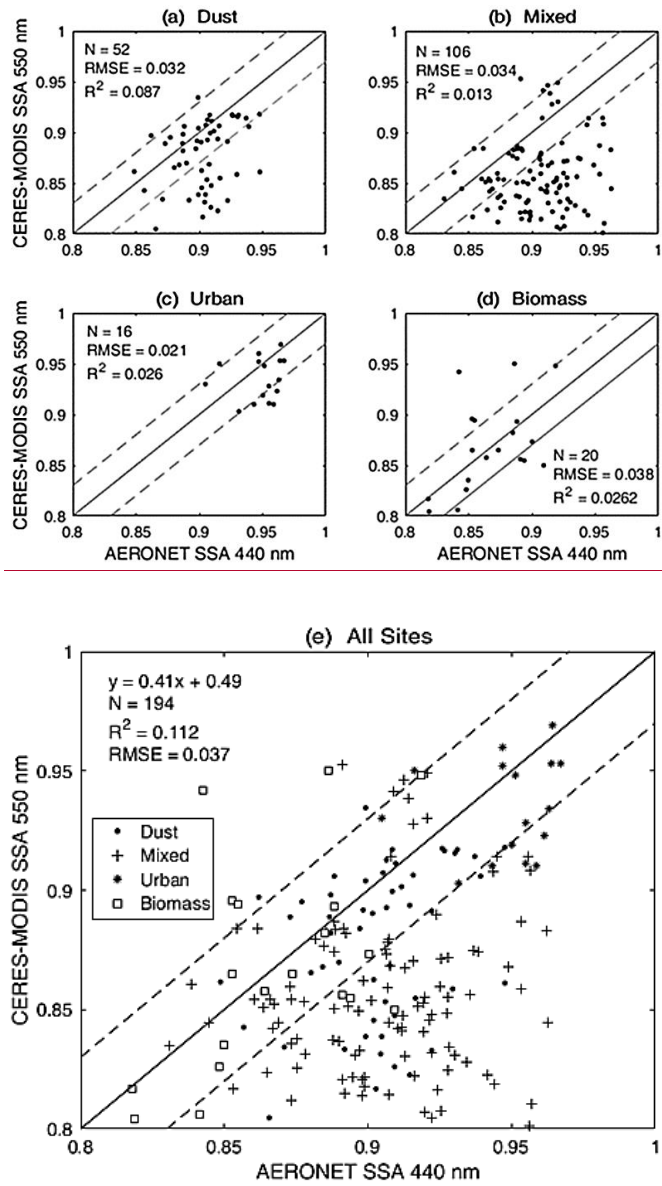
Figure 7. CERES-MODIS SSA (550 nm) vs AERONET SSA (440 nm) for various AERONET sites classified based on type of aerosols (Giles et al., 2012)

8. Summary and Conclusions

Deleted: 6

- Global maps of aerosol absorption have been generated following the concept of "critical optical depth".

- The retrieved SSA values have been compared with available aircraft measurements. The limited comparison exercise shows that most of the retrieved SSA values are within ±0.03.

Deleted: validated by comparing against
Deleted: validation

- We show that the combined CERES-MODIS algorithm better captures the spatial and seasonal variations in aerosol absorption and the resultant maps provide an improved global SSA database with fewer data gaps. Global mean SSA was estimated to be 0.93 and 0.97 over land and ocean, respectively

- The algorithm's sensitivity to various parameters have been studied, which shows maximum sensitivity to changes in surface albedo. The algorithm is shown to be the most effective over regions with large AOD variations and less surface albedo variations.

Deleted: The uncertainty analysis shows typical uncertainty of ±0.03
Deleted: with

- Comparison with SSA from 15 AERONET sites showed an acceptable agreement between AERONET and CERES-MODIS SSA, within their uncertainties.

- Overall, the combined CERES-MODIS algorithm provides global SSA maps with improved accuracy and better spatial coverage. These global maps provide valuable input for models to make assessment of aerosol-climate impacts on both regional and global scales.

Data Availability

MODIS and CERES data used in this study are available at https://asdc.larc.nasa.gov/. The combined CERES-MODIS datasets are available upon request from the corresponding author.

Author Contributions

SKS conceptualized the method. AD developed the algorithm, carried out the simulations, and analyzed the data. AD wrote the manuscript with revisions from SKS.

Competing interests

The authors declare they have no conflict of interest.

Acknowledgment

The authors gratefully acknowledge the Atmospheric Science Data Center (ASDC) at NASA's Earth Observing System Data and Information System (EOSDIS) Distributed Active Archive Centers (DAACs) for providing MODIS, OMI, and CERES data products used in this study.   In addition, one of the authors (S. K. Satheesh) acknowledges the JC Bose Fellowship awarded to him by SERB-Department of Science and Technology, New Delhi. This study is supported by "Tata Education and Development Trust."

References

Ahn, C., Torres, O. and Jethva, H.: Assessment of OMI near-UV aerosol optical depth over land, J. Geophys. Res. Atmos., 119(5), 2457–2473, https://doi.org/10.1002/2013JD020188, 2014.

Anderson, T. L., Charlson, R. J., Bellouin, N., Boucher, O., Chin, M., Christopher, S. A., Haywood, J., Kaufman, Y. J., Kinne, S., Ogren, J. A., Remer, L. A., Takemura, T., Tanré, D., Torres, O., Trepte, C. R., Wielicki, B. A., Winker, D. M. and Yu, H.: An "a-train"strategy for quantifying direct climate forcing by anthropogenic aerosols, Bull. Am. Meteorol. Soc., 86(12), 1795–1809, doi:10.1175/BAMS-86-12-1795, 2005.

Anderson, T. L., Covert, D. S., Marshall, S. F., Laucks, M. L., Charlson, R. J., Waggoner, A. P., Ogren, J. A., Caldow, R., Holm, R. L., Quant, F. R., Sem, G. J., Wiedensohler, A., Ahlquist, N. A., and Bates, T. S.: Performance Characteristics of a High-Sensitivity, Three-Wavelength, Total Scatter/Backscatter Nephelometer, J. Atmos. Ocean. Technol., 13, 967–986, https://doi.org/10.1175/1520-0426(1996)013, 1996.

Babu, S. S., Moorthy, K. K., Manchanda, R. K., Sinha, P. R., Satheesh, S. K., Vajja, D. P., Srinivasan, S. and Kumar, V. H. A.: Free tropospheric black carbon aerosol measurements using high altitude balloon: Do BC layers

build "their own homes"up in the atmosphere?, Geophys. Res. Lett., 38(8), doi:10.1029/2011GL046654, 2011.

Babu, S. S., Nair, V. S., Gogoi, M. M. and Moorthy, K. K.: Seasonal variation of vertical distribution of aerosol single scattering albedo over Indian sub-continent: RAWEX aircraft observations, Atmos. Environ., 125, 312–323, doi:10.1016/j.atmosenv.2015.09.041, 2016.

5   Bergstrom, R. W., Pilewskie, P., Schmid, B. and Russell, P. B.: Estimates of the spectral aerosol single scattering albedo and aerosol radiative effects during SAFARI 2000, J. Geophys. Res. Atmos., 108(D13), https://doi.org/10.1029/2002JD002435, 2003.

IPCC – Intergovernmental Panel on Climate Change: The physical science basis: Contribution of Working Group I to the Fifth Assessment Report of the Intergovernmental Panel on Climate Change, in: Climate Change (2013),
10   edited by: Stocker, T. F., Qin, D., Plattner, G. K., Tignor, M., Allen, S. K., Boschung, J., Nauels, A., Xia, Y., Bex, V., and Midgley, P. M., Cambridge University, Press, Cambridge, UK and New York, NY, USA, 1535 pp., https://doi.org/10.1017/CBO9781107415324, 2013.

Chand, D., Wood, R., Anderson, T. L., Satheesh, S. K., and Charlson, R. J.: Satellite-derived direct radiative effect of aerosols dependent on cloud cover, Nat. Geosci., 2, 181–184, https://doi.org/10.1038/ngeo437, 2009.

15   Chu, D. A., Kaufman, Y. J., Ichoku, C., Remer, L. A., Tanré, D., and Holben, B. N.: Validation of MODIS aerosol optical depth retrieval over land, Geophys. Res. Lett., 29, MOD2-1, https://doi.org/10.1029/2001GL013205, 2002

Deepshikha, S., Satheesh, S. K. and Srinivasan, J.: Regional distribution of absorbing efficiency of dust aerosols over India and adjacent continents inferred using satellite remote sensing, Geophys. Res. Lett., 32(3), 1–4, doi:10.1029/2004GL022091, 2005.

20   Dubovik, O., Holben, B., Eck, T. F., Smirnov, A., Kaufman, Y. J., King, M. D., Tanré, D., and Slutsker, I.: Variability of Absorption and Optical Properties of Key Aerosol Types Observed in Worldwide Locations. Journal of the Atmospheric Sciences 59, 3, 590-608, https://doi.org/10.1175/1520-0469(2002)059<0590:VOAAOP>2.0.CO;2, 2002

Eswaran, K., Satheesh, S. K. and Srinivasan, J.: Multi-satellite retrieval of single scattering albedo using the OMI–
25   MODIS algorithm, Atmos. Chem. Phys., 19(5), 3307–3324, doi:10.5194/acp-19-3307-2019, 2019.

Fraser, R. S. and Kaufman, Y. J, "The Relative Importance of Aerosol Scattering and Absorption in Remote Sensing," in IEEE Transactions on Geoscience and Remote Sensing, vol. GE-23, no. 5, pp. 625-633, Sept. 1985, doi: 10.1109/TGRS.1985.289380.

Giles, D. M., Holben, B. N., Eck, T. F., Sinyuk, A., Smirnov, A., Slutsker, I., Dickerson, R. R., Thompson, A. M.,
30   and Schafer, J. S.: An analysis of AERONET aerosol absorption properties and classifications representative of aerosol source regions, J. Geophys. Res. Atmos., 117, 17203, https://doi.org/10.1029/2012JD018127, 2012.

Govardhan, G., Satheesh, S. K., Moorthy, K. K. and Nanjundiah, R.: Simulations of black carbon over the Indian region: improvements and implications of diurnality in emissions, Atmos. Chem. Phys., 19(12), 8229–8241,

doi:10.5194/acp-19-8229-2019, 2019.

Haywood, J. M., Francis, P. N., Glew, M. D. and Taylor, J. P.: Optical properties and direct radiative effect of Saharan dust: A case study of two Saharan dust outbreaks using aircraft data, J. Geophys. Res. Atmos., 106(D16), 18417–18430, doi:10.1029/ 2000JD900319 @10.1002/ (ISSN)2169-8996.DUST1, 2001.

5   Hammer, M. S., Martin, R. V., Li, C., Torres, O., Manning, M., and Boys, B. L.: Insight into global trends in aerosol composition from 2005 to 2015 inferred from the OMI Ultraviolet Aerosol Index, Atmos. Chem. Phys., 18, 8097–8112, https://doi.org/10.5194/acp-18-8097-2018, 2018.

Hsu, N. C., Herman, J. R. and Weaver, C.: Determination of radiative forcing of Saharan dust using combined TOMS and ERBE data, J. Geophys. Res. Atmos., 105(16), 20649–20661, doi:10.1029/2000jd900150, 2000.

10   Hsu, N. C., Tsay, S. C., King, M. D. and Herman, J. R.: Aerosol properties over bright-reflecting source regions, IEEE Trans. Geosci. Remote Sens., 42(3), 557–569, doi:10.1109/TGRS.2004.824067, 2004.

Hsu, N. C., Jeong, M. J., Bettenhausen, C., Sayer, A. M., Hansell, R., Seftor, C. S., Huang, J., and Tsay, S. C.: Enhanced Deep Blue aerosol retrieval algorithm: The second generation, J. Geophys. Res. Atmos., 118, 9296–9315, https://doi.org/10.1002/jgrd.50712, 2013.

15   Hu, R. -M., Martin, R. V. and Fairlie, T. D.: Global retrieval of columnar aerosol single scattering albedo from space-based observations, J. Geophys. Res. Atmos., 112(D2), doi:10.1029/2005JD006832, 2007.

Hu, R. M., Sokhi, R. S. and Fisher, B. E. A.: New algorithms and their application for satellite remote sensing of surface PM2.5 and aerosol absorption, J. Aerosol Sci., 40(5), 394–402, doi:10.1016/j.jaerosci.2009.01.005, 2009.

Jeong, M. J., Li, Z., Chu, D. A., and Tsay, S. C.: Quality and compatibility analyses of global aerosol products
20   derived from the advanced very high resolution radiometer and Moderate Resolution Imaging Spectroradiometer, J. Geophys. Res. Atmos., 110, 1–16, https://doi.org/10.1029/2004JD004648, 2005.

Jeong, M. J. and Hsu, N. C.: Retrievals of aerosol single-scattering albedo and effective aerosol layer height for biomass-burning smoke: Synergy derived from "A-Train" sensors, Geophys. Res. Lett., 35(24), L24801, doi:10.1029/2008GL036279, 2008.

25   Jethva, H., Torres, O., and Ahn, C.: A 12-year long global record of optical depth of absorbing aerosols above the clouds derived from the OMI/OMACA algorithm, Atmos. Meas. Tech., 11, 5837–5864, https://doi.org/10.5194/amt-11-5837-2018, 2018.

Jethva, H. and Torres, O.: A comparative evaluation of Aura-OMI and SKYNET near-UV single-scattering albedo products, Atmos. Meas. Tech., 12(12), 6489–6503, https://doi.org/10.5194/amt-12-6489-2019, 2019.

30   Justice, C. O., Kendall, J. D., Dowty, P. R. and Scholes, R. J.: Satellite remote sensing of fires during the SAFARI campaign using NOAA Advanced Very High Resolution Radiometer data, J. Geophys. Res. Atmos., 101(D19), 23851–23863, https://doi.org/10.1029/95JD00623, 1996.

Kaufman, Y. J.: Satellite sensing of aerosol absorption., J. Geophys. Res., 92(D4), 4307–4317, doi:10.1029/JD092iD04p04307, 1987.

Kaufman, Y. J. and Joseph, J. H.: Determination of surface albedos and aerosol extinction characteristics from satellite imagery., J. Geophys. Res., 87(C2), 1287–1299, https://doi.org/10.1029/JC087iC02p01287, 1982.

5   Kaufman, Y. J., Fraser, R. S., and Ferrare, R. A.: Satellite measurements of large-scale air pollution: methods, J. Geophys. Res., 95, 9895–9909, https://doi.org/10.1029/JD095iD07p09895, 1990.

Kaufman, Y. J., Tanré, D., Dubovik, O., Karnieli, A., and Remer, L. A.: Absorption of sunlight by dust as inferred from satellite and ground-based remote sensing, Geophys. Res. Lett., 28, 1479–1482, https://doi.org/10.1029/2000GL012647, 2001.

10   Kaufman, Y. J., Tanré, D. and Boucher, O.: A satellite view of aerosols in the climate system, Nature, 419(6903), 215–223, https://doi.org/10.1038/nature01091, 2002.

Kaufman, Y. J., Tanré, D., Dubovik, O., Karnieli, A. and Remer, L. A.: Absorption of sunlight by dust as inferred from satellite and ground-based remote sensing, Geophys. Res. Lett., 28(8), 1479–1482, doi:10.1029/2000GL012647, 2001.

15   Lenoble, J., Remer, L. and Tanre, D. eds.: Aerosol remote sensing. Springer Science & Business Media, 2013.

Levy, R. C., Remer, L. A., Mattoo, S., Vermote, E. F. and Kaufman, Y. J.: Second-generation operational algorithm: Retrieval of aerosol properties over land from inversion of Moderate Resolution Imaging Spectroradiometer spectral reflectance, J. Geophys. Res. Atmos., 112(13), doi:10.1029/2006JD007811, 2007.

Levy, R. C., Remer, L. A., and Dubovik, O.: Global aerosol optical properties and application to Moderate
20   Resolution Imaging Spectroradiometer aerosol retrieval over land, J. Geophys. Res. Atmos., 112, 13210, https://doi.org/10.1029/2006JD007815, 2007.Levy, R. C., Mattoo, S., Munchak, L. A., Remer, L. A., Sayer, A. M., Patadia, F. and Hsu, N. C.: The Collection 6 MODIS aerosol products over land and ocean, Atmos. Meas. Tech., 6(11), 2989–3034, doi:10.5194/amt-6-2989-2013, 2013.

Manoj, M. R., Satheesh, S. K., Moorthy, K. K. and Coe, H.: Vertical profiles of sub-micron aerosol single
25   scattering albedo over Indian region immediately before monsoon onset and during its development: Research from the SWAAMI field campaign, Atmos. Chem. Phys. Discuss., 1–29, doi:10.5194/acp-2019-657, 2019.

Moorthy, K. K., Satheesh, S. K. and Kotamarthi, V. R.: Evolution of aerosol research in India and the RAWEX–GVAX: an overview, Curr. Sci., 111, 53–75, doi:10.2307/24910009, 2016.

Nair, V. S., Krishna Moorthy, K., Suresh Babu, S., and Satheesh, S. K.: Optical and Physical Properties of
30   Atmospheric Aerosols over the Bay of Bengal during ICARB, J. Atmos. Sci., 66, 2640–2658, https://doi.org/10.1175/2009JAS3032.1, 2009.

Narasimhan, D. and Satheesh, S. K.: Estimates of aerosol absorption over India using multi-satellite retrieval,

Ann. Geophys., 31(10), 1773–1778, doi:10.5194/angeo-31-1773-2013, 2013.

Remer, L. A., Tanré, D., Kaufman, Y. J., Ichoku, C., Mattoo, S., Levy, R., Chu, D. A., Holben, B., Dubovik, O., Smirnov, A., Martins, J. V., Li, R. R., and Ahmad, Z.: Validation of MODIS aerosol retrieval over ocean, Geophys. Res. Lett., 29, MOD3-1, https://doi.org/10.1029/2001GL013204, 2002.

5   Remer, L. A., Kleidman, R. G., Levy, R. C., Kaufman, Y. J., Tanré, D., Mattoo, S., Martins, J. V., Ichoku, C., Koren, I., Yu, H., and Holben, B. N.: Global aerosol climatology from the MODIS satellite sensors, J. Geophys. Res. Atmos., 113, 14–21, https://doi.org/10.1029/2007JD009661, 2008.

Rutan, D. A., Kato, S., Doelling, D. R., Rose, F. G., Nguyen, L. T., Caldwell, T. E. and Loeb, N. G.: CERES Synoptic Product: Methodology and Validation of Surface Radiant Flux, J. Atmos. Ocean. Technol., 32(6), 1121–
10   1143, doi:10.1175/JTECH-D-14-00165.1, 2015.

Satheesh, S. K. and Srinivasan, J.: A method to infer short wave absorption due to aerosols using satellite remote sensing, Geophys. Res. Lett., 32(13), 1–4, doi:10.1029/2005GL023064, 2005.

Satheesh, S. K., Krishna Moorthy, K., Suresh Babu, S., Vinoj, V. and Dutt, C. B. S.: Climate implications of large warming by elevated aerosol over India, Geophys. Res. Lett., 35(19), L19809, doi:10.1029/2008GL034944, 2008.

15   Satheesh, S. K., Torres, O., Remer, L. A., Babu, S. S., Vinoj, V., Eck, T. F., Kleidman, R. G. and Holben, B. N.: Improved assessment of aerosol absorption using OMI-MODIS joint retrieval, J. Geophys. Res. Atmos., 114(5), D05209, doi:10.1029/2008JD011024, 2009.

Sayer, A. M., Hsu, N. C., Bettenhausen, C. and Jeong, M. J.: Validation and uncertainty estimates for MODIS Collection 6 "deep Blue"aerosol data, J. Geophys. Res. Atmos., 118(14), 7864–7872, doi:10.1002/jgrd.50600,
20   2013.

Seidel, F. C. and Popp, C.: Critical surface albedo and its implications to aerosol remote sensing, Atmos. Meas. Tech., 5, 1653–1665, https://doi.org/10.5194/AMT-5-1653-2012, 2012.

Stamnes, K., Tsay, S.-C., Wiscombe, W. and Jayaweera, K.: Numerically stable algorithm for discrete-ordinate-method radiative transfer in multiple scattering and emitting layered media, Appl. Opt., 27(12), 2502,
25   doi:10.1364/ao.27.002502, 1988.

Torres, O., Bhartia, P. K., Herman, J. R., Sinyuk, A., Ginoux, P. and Holben, B.: A long-term record of aerosol optical depth from TOMS observations and comparison to AERONET measurements, J. Atmos. Sci., 59(3 PT 1), 398–413, https://doi.org/10.1175/1520-0469(2002)059<0398:altroa>2.0.co;2, 2002.

Torres, O., Bhartia, P.K., Sinyuk, A., Welton, E.J. and Holben, B.: Total Ozone Mapping Spectrometer
30   measurements of aerosol absorption from space: Comparison to SAFARI 2000 ground-based observations. Journal of Geophysical Research: Atmospheres, 110(D10), 2005.

Torres, O., Tanskanen, A., Veihelmann, B., Ahn, C., Braak, R., Bhartia, P. K., Veefkind, P., and Levelt, P.:

Aerosols and surface UV products from Ozone Monitoring Instrument observations: An overview, J. Geophys. Res. Atmos., 112, https://doi.org/10.1029/2007JD008809@10.1002/(ISSN)2169-8996.AURA1, 2007.

Torres, O., Ahn, C. and Chen, Z.: Improvements to the OMI near-UV aerosol algorithm using A-train CALIOP and AIRS observations, Atmos. Meas. Tech., 6(11), 3257–3270, https://doi.org/10.5194/amt-6-3257-2013, 2013.

5 Vaishya, A., Babu, S. N. S., Jayachandran, V., Gogoi, M. M., Lakshmi, N. B., Moorthy, K. K. and Satheesh, S. K.: Large contrast in the vertical distribution of aerosol optical properties and radiative effects across the Indo-Gangetic Plain during the SWAAMI–RAWEX campaign, Atmos. Chem. Phys., 18(23), 17669–17685, doi:10.5194/acp-18-17669-2018, 2018.

Wells, K. C., Martins, J. V., Remer, L. A., Kreidenweis, S. M., and Stephens, G. L.: Critical reflectance derived
10 from MODIS: Application for the retrieval of aerosol absorption over desert regions, J. Geophys. Res. Atmos., 117, 3202, https://doi.org/10.1029/2011JD016891, 2012.

Wielicki, B. A., Barkstrom, B. R., Harrison, E. F., Lee, R. B., Smith, G. L. and Cooper, J. E.: Clouds and the Earth's Radiant Energy System (CERES): An Earth Observing System Experiment, Bull. Am. Meteorol. Soc., 77(5), 853–868, doi:10.1175/1520-0477(1996)077<0853:CATERE>2.0.CO;2, 1996.

15 Wooster, M. J.: Boreal forest fires burn less intensely in Russia than in North America, Geophys. Res. Lett., 31(20), L20505, https://doi.org/10.1029/2004GL020805, 2004.

Zhu, L., Martins, J. V. and Remer, L. A.: Biomass burning aerosol absorption measurements with MODIS using the critical reflectance method, J. Geophys. Res. Atmos., 116(7), D07202, doi:10.1029/2010JD015187, 2011.

Supplementary Material

Global maps of aerosol single scattering albedo using combined CERES-MODIS retrieval

Archana Devi[1], Sreedharan K Satheesh[1,2,3]

[1] Centre for Atmospheric and Oceanic Sciences, Indian Institute of Science, Bengaluru, India
[2] Divecha Centre for Climate Change, Indian Institute of Science, Bengaluru, India
[3] DST Centre of Excellence in Climate Change, Indian Institute of Science, Bengaluru, India

Correspondence to: Archana Devi (archana.shiva13@gmail.com)
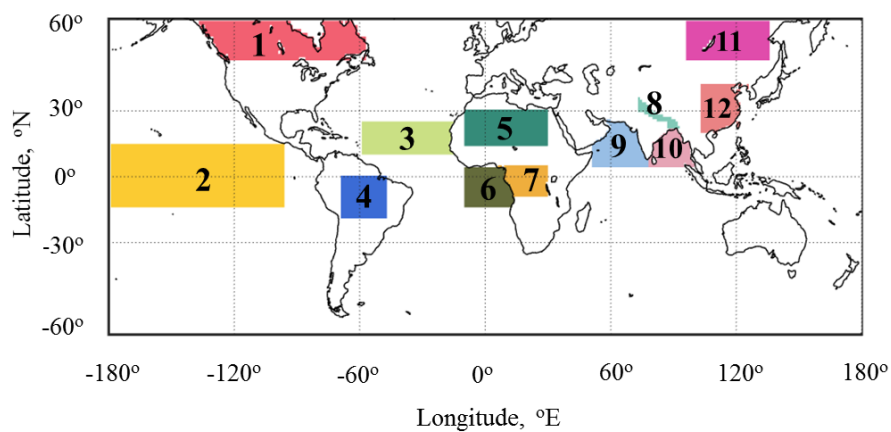
Figure S1. Regions of interest (ROI). Details of each region are provided in Table S1

Table S1. Details of the regions shown in Fig. S1

ROI No:	Region	General aerosol characteristics	Lat limit, °N	Lon limit, °E
1	Canadian Boreal Forest	Relatively pristine with seasonal biomass burning	48 to 60	-140 to -58
2	Eastern Pacific	Less polluted oceanic region	-15 to 15	-180 to -97
3	North East Atlantic	Highly polluted by dust transport and continental outflow from biomass burning	10 to 25	-60 to -10
4	Amazon	Relatively pristine with seasonal biomass burning	-20 to 0	-70 to -48
5	Sahara	Desert region with seasonal dust storms	14 to 30	-11 to 28
6	Southeast Atlantic	Highly polluted by dust transport and continental outflow from biomass burning	-15 to 4	-11 to 15
7	South African Forest	Relatively pristine with seasonal biomass burning	-10 to 5	3 to 29
8	Indo Gangetic Plain	A highly polluted industrial region with seasonal stubble burning and dust from the Thar desert	22 to 35	72 to 92
9	Arabian Sea	Continental outflow of pollution and dust	4 to 26	50 to 77
10	Bay of Bengal	Continental outflow of pollution	4 to 24	77 to 99
11	Russian Boreal Forest	Relatively pristine with seasonal biomass burning	48 to 60	95 to 135
12	Eastern China	A highly polluted industrial region	20 to 40	102 to 125

Table S2. Seasonal mean SSA over regions of interest from combined CERES-MODIS, OMI (given in round brackets) and POLDER (given in square brackets). Details of these regions are given in Table S1 and Fig. S1

Region	CERES-MODIS SSA 550 nm (OMI SSA 500 nm) [POLDER SSA 565 nm]			
	DJF	MAM	JJA	SON
Canadian Boreal Forest	NODATA (0.95 ± 0.02) [0.96 ± 0.04]	0.96 ± 0.02 (0.94 ± 0.01) [0.84 ± 0.05]	0.91 ± 0.02 (0.94 ± 0.01) [0.89 ± 0.04]	0.94 ± 0.02 (0.93 ± 0.01) [0.90 ± 0.05]
Russian Boreal Forest	NO DATA (0.95 ± 0.02) [0.81 ± 0.08]	0.96 ± 0.02 (0.94 ± 0.01) [0.89 ± 0.03]	0.90 ± 0.01 (0.94 ± 0.01) [0.91 ± 0.03]	0.96 ± 0.01 (0.93 ± 0.01) [0.89 ± 0.05]
South African Forest	0.91 ± 0.02 (0.93 ± 0.01) [0.84 ± 0.03]	0.92 ± 0.01 (0.94 ± 0.01) [0.90 ± 0.03]	0.83 ± 0.01 (0.93 ± 0.02) [0.88 ± 0.03]	0.90 ± 0.01 (0.94 ± 0.01) [0.85 ± 0.05]
Amazon Forest	0.96 ± 0.02 (0.95 ± 0.01) [0.84 ± 0.07]	0.98 ± 0.01 (0.95 ± 0.01) [0.91 ± 0.05]	0.97 ± 0.02 (0.93 ± 0.01) [0.92 ± 0.02]	0.89 ± 0.02 (0.94 ± 0.01) [0.87 ± 0.04]
North East Atlantic	0.96 ± 0.02 (0.90 ± 0.01) [0.94 ± 0.03]	0.94 ± 0.02 (0.92 ± 0.01) [0.93 ± 0.01]	0.92 ± 0.02 (0.95 ± 0.01) [0.93 ± 0.02]	0.93 ± 0.03 (0.94 ± 0.01) [0.94 ± 0.01]
South East Atlantic	0.92 ± 0.02 (0.92 ± 0.01) [0.88 ± 0.04]	0.94 ± 0.02 (0.92 ± 0.01) [0.94 ± 0.01]	0.89 ± 0.01 (0.91 ± 0.01) [0.88 ± 0.03]	0.92 ± 0.02 (0.94 ± 0.01) [0.89 ± 0.03]
Eastern Pacific	0.97 ± 0.01 (0.94 ± 0.02) [0.97 ± 0.01]	0.97 ± 0.01 (0.95 ± 0.02) [0.95 ± 0.02]	0.96 ± 0.01 (0.95 ± 0.02) [0.95 ± 0.02]	0.97 ± 0.01 (0.95 ± 0.02) [0.93 ± 0.03]
Sahara	0.93 ± 0.01 (0.92 ± 0.01) [0.90 ± 0.03]	0.93 ± 0.01 (0.93 ± 0.01) [0.88 ± 0.03]	0.91 ± 0.02 (0.94 ± 0.01) [0.87 ± 0.04]	0.92 ± 0.02 (0.93 ± 0.01) [0.90 ± 0.03]
Indo Gangetic Plain	0.88 ± 0.01 (0.92 ± 0.01) [0.89 ± 0.01]	0.87 ± 0.01 (0.92 ± 0.01) [0.83 ± 0.02]	0.85 ± 0.02 (0.95 ± 0.01) [0.77 ± 0.03]	0.83 ± 0.01 (0.92 ± 0.01) [0.89 ± 0.01]
Eastern China	0.92 ± 0.01 (0.92 ± 0.01) [0.91 ± 0.01]	0.90 ± 0.01 (0.94 ± 0.01) [0.87 ± 0.02]	0.87 ± 0.01 (0.95 ± 0.01) [0.84 ± 0.04]	0.88 ± 0.02 (0.93 ± 0.01) [0.91 ± 0.03]
Arabian Sea	0.92 ± 0.01 (0.91 ± 0.02) [0.94 ± 0.02]	0.89 ± 0.01 (0.93 ± 0.01) [0.92 ± 0.02]	0.91 ± 0.01 (0.96 ± 0.01) [0.94 ± 0.02]	0.89 ± 0.01 (0.93 ± 0.02) [0.93 ± 0.02]
Bay of Bengal	0.91 ± 0.01 (0.92 ± 0.01) [0.93 ± 0.02]	0.90 ± 0.01 (0.94 ± 0.01) [0.91 ± 0.02]	0.91 ± 0.02 (0.95 ± 0.01) [0.95 ± 0.02]	0.91 ± 0.02 (0.94 ± 0.02) [0.93 ± 0.03]
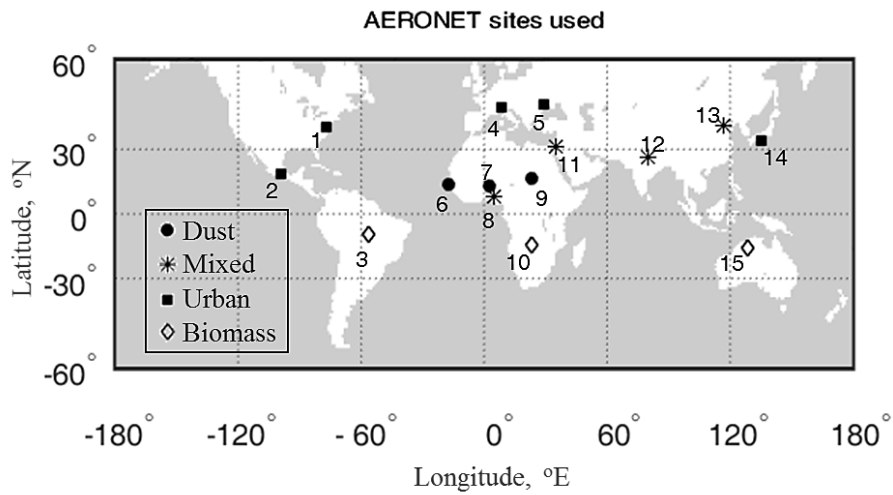
Figure S2. Map showing location of AERONET sites used in this study. The type of aerosols (dust, mixed, urban and biomass) were as defined in Giles et al., 2012

Table S3: Name of AERONET site as shown in Fig. S2

No.	Name	No.	Name	No.	Name
1	GSFC	6	Capo_Verde	11	SEDE_BOKER
2	Mexico_City	7	Dakar	12	Kanpur
3	Alta_Floresta	8	Illorin	13	XiangHe
4	Ispra	9	Banizoumbou	14	Shirahama
5	Moldova	10	Mongu	15	Lake_Argyle
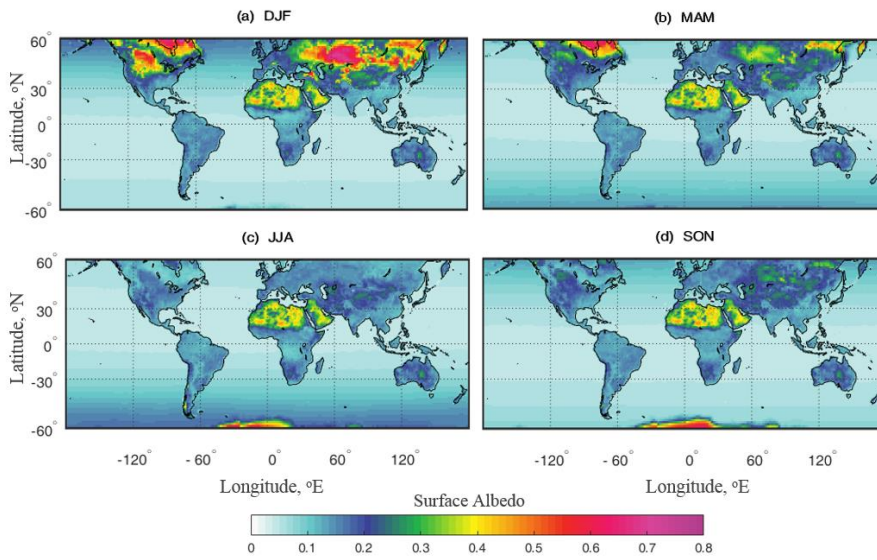
Figure S3. Seasonal mean shortwave-integrated surface albedo from CERES

Table S4. Shortwave integrated seasonal mean surface albedo from CERES over regions of interest. Details of these regions are given in Table S1 and Fig. S1

Region	Surface Albedo			
	DJF	MAM	JJA	SON
Canadian Boreal Forest	0.36 ± 0.13	0.30 ± 0.12	0.12 ± 0.03	0.16 ± 0.05
Russian Boreal Forest	0.37 ± 0.10	0.27 ± 0.08	0.13 ± 0.02	0.20 ± 0.05
South African Forest	0.12 ± 0.01	0.13 ± 0.01	0.12 ± 0.02	0.13 ± 0.01
Amazon Forest	0.14 ± 0.01	0.14 ± 0.01	0.13 ± 0.02	0.14 ± 0.02
North East Atlantic	0.06 ± 0.01	0.05 ± 0.01	0.05 ± 0.01	0.05 ± 0.01
South East Atlantic	0.05 ± 0.01	0.05 ± 0.01	0.05 ± 0.01	0.05 ± 0.01
Eastern Pacific	0.05 ± 0.01	0.05 ± 0.00	0.05 ± 0.01	0.05 ± 0.00
Sahara	0.35 ± 0.06	0.34 ± 0.06	0.34 ± 0.06	0.34 ± 0.06
Indo Gangetic Plain	0.13 ± 0.02	0.13 ± 0.02	0.14 ± 0.02	0.13 ± 0.01
Eastern China	0.13 ± 0.04	0.13 ± 0.03	0.13 ± 0.03	0.13 ± 0.03
Arabian Sea	0.06 ± 0.01	0.05 ± 0.01	0.05 ± 0.02	0.05 ± 0.01
Bay of Bengal	0.05 ± 0.01	0.05 ± 0.01	0.05 ± 0.01	0.05 ± 0.01

Formatted Table

Table S5: Normalized extinction coefficient of the aerosol model

λ (μm)	Ext$_{norm}$	λ (μm)	Ext$_{norm}$	λ (μm)	Ext$_{norm}$
0.25	1.597	0.75	0.847	3.2	0.5075
0.3	1.467	0.8	0.8202	3.39	0.5047
0.35	1.334	0.9	0.7828	3.5	0.5062
0.4	1.224	1	0.7536	3.75	0.4828
0.45	1.135	1.25	0.7038	4	0.4629
0.5	1.061	1.5	0.6706	4.5	0.4395
0.55	1	1.75	0.6349	5	0.4103
0.6	0.9505	2	0.5883		
0.65	0.9106	2.5	0.4905		
0.7	0.8757	3	0.491		

Table S6: Phase function of the aerosol model (continued into Table S7)

λ (μm)	Streams							
	1	2	3	4	5	6	7	8
0.25	0.754	0.606	0.473	0.397	0.342	0.307	0.283	0.265
0.3	0.738	0.589	0.452	0.379	0.325	0.293	0.270	0.254
0.35	0.738	0.592	0.456	0.386	0.333	0.303	0.279	0.264
0.4	0.741	0.598	0.463	0.395	0.343	0.313	0.290	0.275
0.45	0.743	0.602	0.468	0.403	0.351	0.323	0.299	0.284
0.5	0.746	0.607	0.474	0.411	0.359	0.331	0.308	0.292
0.55	0.748	0.611	0.478	0.416	0.364	0.337	0.313	0.297
0.6	0.749	0.615	0.481	0.421	0.368	0.342	0.317	0.301
0.65	0.750	0.618	0.485	0.426	0.373	0.347	0.321	0.305
0.7	0.751	0.620	0.487	0.429	0.376	0.350	0.323	0.306
0.75	0.752	0.623	0.490	0.433	0.378	0.352	0.325	0.308
0.8	0.755	0.628	0.494	0.437	0.382	0.355	0.327	0.310
0.9	0.756	0.631	0.496	0.440	0.383	0.356	0.326	0.308
1	0.756	0.632	0.496	0.440	0.382	0.354	0.323	0.304
1.25	0.766	0.643	0.505	0.442	0.380	0.346	0.314	0.291
1.5	0.777	0.651	0.512	0.441	0.376	0.337	0.302	0.276
1.75	0.798	0.673	0.536	0.455	0.385	0.339	0.300	0.271
2	0.826	0.707	0.577	0.491	0.415	0.362	0.316	0.282
2.5	0.858	0.750	0.636	0.552	0.476	0.418	0.365	0.323
3	0.871	0.765	0.662	0.578	0.505	0.444	0.391	0.346
3.2	0.836	0.708	0.584	0.491	0.414	0.354	0.304	0.264
3.39	0.818	0.682	0.548	0.453	0.375	0.317	0.270	0.233
3.5	0.808	0.670	0.530	0.434	0.356	0.299	0.253	0.217
3.75	0.805	0.667	0.524	0.429	0.349	0.292	0.246	0.210
4	0.797	0.660	0.513	0.421	0.340	0.284	0.238	0.202
4.5	0.795	0.655	0.507	0.413	0.331	0.275	0.228	0.192
5	0.808	0.663	0.520	0.420	0.338	0.278	0.230	0.192

Table S7: Phase function of aerosol model

λ (μm)	Streams							
	9	10	11	12	13	14	15	16
0.25	0.252	0.241	0.233	0.226	0.219	0.214	0.209	0.204
0.3	0.241	0.232	0.224	0.217	0.211	0.205	0.200	0.196
0.35	0.251	0.242	0.233	0.226	0.219	0.214	0.208	0.203
0.4	0.262	0.252	0.243	0.235	0.228	0.222	0.216	0.210
0.45	0.270	0.260	0.251	0.242	0.235	0.228	0.221	0.215
0.5	0.278	0.267	0.257	0.248	0.240	0.233	0.226	0.219
0.55	0.283	0.271	0.261	0.251	0.243	0.235	0.227	0.220
0.6	0.286	0.274	0.263	0.253	0.244	0.235	0.228	0.220
0.65	0.289	0.277	0.265	0.255	0.245	0.236	0.228	0.220
0.7	0.290	0.277	0.265	0.254	0.244	0.235	0.226	0.218
0.75	0.291	0.277	0.265	0.253	0.243	0.233	0.225	0.216
0.8	0.292	0.278	0.265	0.253	0.242	0.232	0.223	0.214
0.9	0.289	0.274	0.261	0.248	0.237	0.226	0.217	0.208
1	0.284	0.269	0.254	0.241	0.230	0.219	0.209	0.200
1.25	0.271	0.253	0.238	0.224	0.212	0.200	0.190	0.180
1.5	0.255	0.236	0.220	0.205	0.193	0.181	0.171	0.161
1.75	0.246	0.226	0.208	0.193	0.180	0.168	0.157	0.147
2	0.252	0.229	0.208	0.191	0.176	0.163	0.151	0.141
2.5	0.287	0.257	0.231	0.208	0.189	0.172	0.157	0.144
3	0.307	0.274	0.245	0.220	0.198	0.179	0.162	0.148
3.2	0.231	0.203	0.180	0.161	0.144	0.130	0.117	0.107
3.39	0.203	0.178	0.157	0.140	0.125	0.113	0.102	0.093
3.5	0.188	0.165	0.146	0.130	0.116	0.104	0.094	0.085
3.75	0.181	0.157	0.139	0.122	0.109	0.097	0.088	0.079
4	0.174	0.150	0.132	0.116	0.103	0.091	0.082	0.073
4.5	0.164	0.141	0.122	0.107	0.094	0.083	0.073	0.066
5	0.163	0.139	0.120	0.103	0.090	0.079	0.070	0.062